
Numerical Study of the Importance of Shear-Thinning Rheology on Thrombosis in a Centrifugal Blood Pump

December 8, 2023

Candidate 12604

University of Bath

Abstract

As the need for donor hearts for Heart Failure (HF) patients rises and the supply continues to lag behind, Ventricular Assist Devices (VADs) will be a more and more common therapeutic option. These carry a risk of pump thrombosis leading to reduced effectiveness and potential distal stroke. Accurate modelling of thrombosis risks in these devices is therefore critical. Thrombus formation is linked to low shear rate regions where shear thinning effects of blood rheology may not be negligible. Therefore, a shear thinning rheological model, namely the Carreau model, was employed on a steady-state multi-reference frame computational model of the Food and Drug Association (FDA) blood pump. This model was validated against pressure head and Particle Image Velocimetry (PIV) measurements made of the same pump geometry from experiments with a Newtonian blood analog using a Newtonian viscosity model. The affect of shear thinning on thrombus deposition was then characterised by comparing the volume of fluid below a critical shear rate of 250s^{-1} in the rotor and exit. Thrombosis was found to be most likely in low flow rate and pump speed conditions and the shear-thinning model showed a minor reduction in this volume particularly at high flow rate, where it reduced by 1.4 %. Since the shear-thinning effect is low and the Newtonian viscosity model is more conservative, we suggest that omission of shear-thinning rheology in blood pump CFD models is justifiable with respect to predicting thrombosis.

List of Acronyms

CFD Computational Fluid Dynamics. 1–3, 12–19, 26

FDA Food and Drug Association. 1–4, 7, 12, 13, 25

HF Heart Failure. 1, 2

MCSD Mechanical Circulatory Support Device. 2

PIV Particle Image Velocimetry. 1, 8, 12–19, 25, 26

RBC Red Blood Cell. 2, 3

SST Shear Stress Transport. 7, 21

VAD Ventricular Assist Device. 1, 2, 7, 23

WSS Wall Shear Stress. 7–12



Figure 1: A scanning electron microscope image of equine red blood cells stacked in a 'rouleaux' [9].

1 Introduction

Ischaemic heart disease is the leading cause of mortality globally accounting for 16 % of deaths [1]. Amongst this, Heart Failure (HF) is projected to affect 1.05×10^6 people in the U.S. [2]. In some of these cases, heart transplantation may be the only option. However, there is a shortage of available donor hearts meaning that Mechanical Circulatory Support Devices (MCSDs) such as Ventricular Assist Devices (VADs) are necessary to bridge the time between a heart transplant being necessary and a donor heart becoming available. VADs have the potential to help many more patients if blood damage problems can be solved [3, 4]. One such issue is thrombosis. Thrombus formation in a VAD can travel downstream to the brain causing stroke and so patients with VADs fitted are commonly on long-term anti-coagulation (blood thinning) medication to abate this [5]. The high shear rates present in VADs means platelet activation is likely [6], while low-shear is related to platelet deposition and hence thrombosis [7].

In Computational Fluid Dynamics (CFD) studies of VADs, it is commonly assumed that blood behaves as a Newtonian fluid due to the high shear-rates involved with all participants of the Interlaboratory CFD study of the Food and Drug Association (FDA) benchmark blood pump assuming a Newtonian viscosity model [8]. Blood is in fact a suspension of Red Blood Cells (RBCs) in plasma. This gives it a shear-thinning rheology because at low shear-rates, the RBCs aggregate into rouleaux, as Figure 1 shows, increasing the viscosity. At higher shear-rates, the rouleaux break down and the viscosity decreases.

Fraser et al. [1] assumed a Newtonian viscosity model for axial and centrifugal VADs and used a shear stress (τ) of greater than 9 Pa to indicate platelet activation. Assuming a continuum viscosity (μ) of blood of 0.0035 Pa s, this gives a shear rate ($\dot{\gamma}$) of 2570 s^{-1} by the relationship

$$\tau = \mu \cdot \dot{\gamma}. \quad (1)$$

For platelet deposition, Hochareon et al. [7] found areas below a shear rate of 250 s^{-1} corresponded with thrombosis in the 50 cc Penn State Artificial Heart - a value where the increase in blood viscosity may have an effect. Good and Manning [10] incorporated a viscoelastic viscosity model for blood into simulations of the FDA blood pump to determine the effects of this on haemolysis, which is where RBCs separate from the plasma they are suspended in [1]. They found that at lower volume flow rates and pump rotational speeds, the non-Newtonian effects had significant impacts on calculated haemolysis index values. They did not investigate the effects on parameters pertinent to thrombosis such as shear stress. It is therefore clear that further understanding of the effects of blood's non-Newtonian behaviour on thrombosis is needed.

A steady-state numerical model for the FDA blood pump was constructed and validated on pressure head and velocity data from experiments performed by Malinauskas and Hariharan respectively [11, 12] across the range of pump speed and flow rates tested. This was done using a Newtonian viscosity model as the experiments were conducted with a Newtonian blood analog and these simulations were then used as a baseline to compare to the non-Newtonian shear-thinning model that was incorporated thereafter. The effect on dynamic viscosity, velocity profiles, and regions prone to thrombosis was then characterised.

2 Methods

The blood pump geometry used has been taken from the FDA for the Interlaboratory CFD challenge [8] and is shown in Figure 2. It consists of an inlet pipe which connects to a housing containing the rotor. The rotor is 52 mm in diameter and is comprised of four equally spaced blades which are square in cross-section with side-length 3 mm and 18.5 mm long. The rotor connects to an exit pipe via a diffuser.

2.1 Grid Topology

The geometry was split into three parts - the inlet, rotor, and exit - which were discretised into grids separately using Ansys Meshing. The inlet was discretised using hexahedral elements, as Figure 3 shows, as hexahedrons are more volume-efficient than tetrahedral elements for a given element-length meaning fewer elements are needed. In addition, since the flow in the inlet is expected to be uniform, hexahedral elements allow the face-normals to be more aligned with the flow. At the wall, inflation layers were generated to capture the high velocity gradients in the boundary layer.

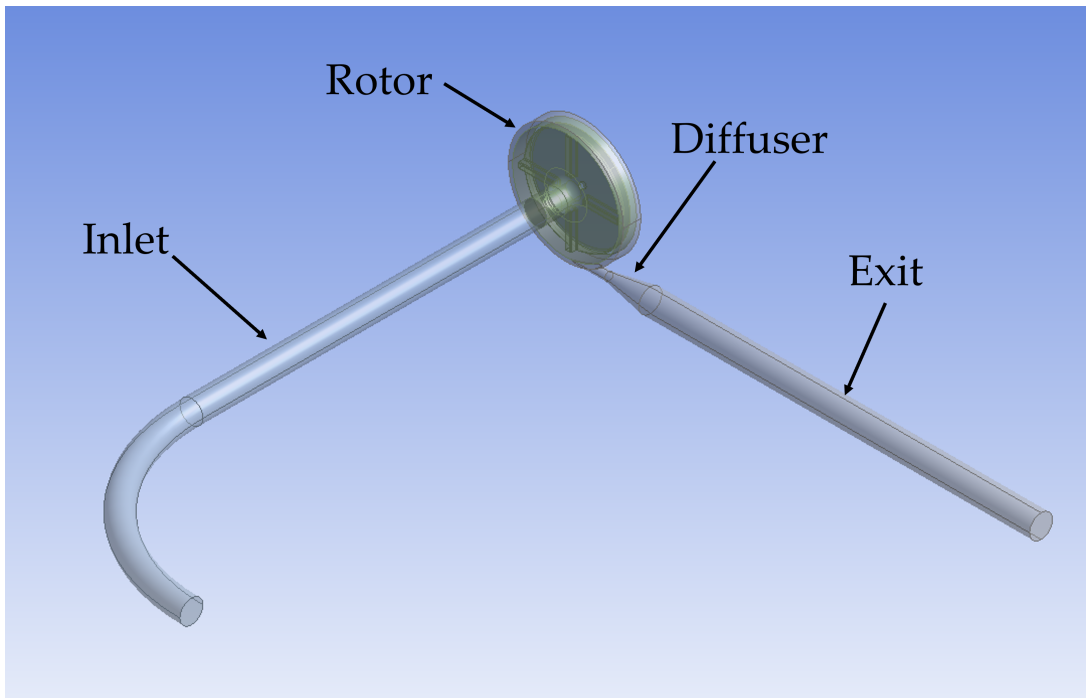


Figure 2: Schematic of the FDA benchmark blood pump geometry used.

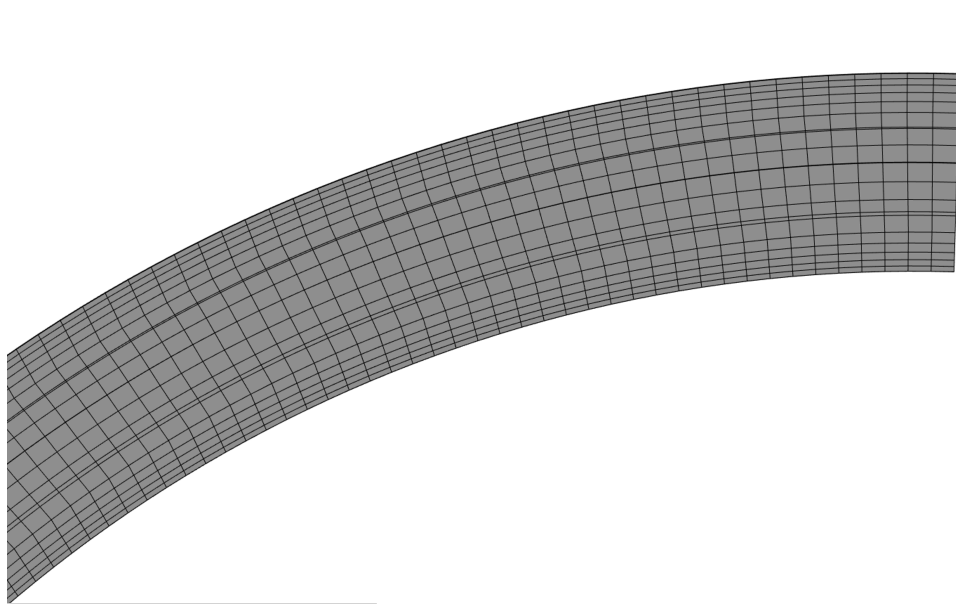


Figure 3: The inlet mesh topology generated using hexahedral elements and inflation layers at the wall.

The rotor was meshed using tetrahedral and prismatic elements due to the complexity of the geometry. The mesh was refined at the rotor surface due to the high velocity gradients expected at this location - particularly at the blades. The rotor mesh topology is shown in Figure 4.

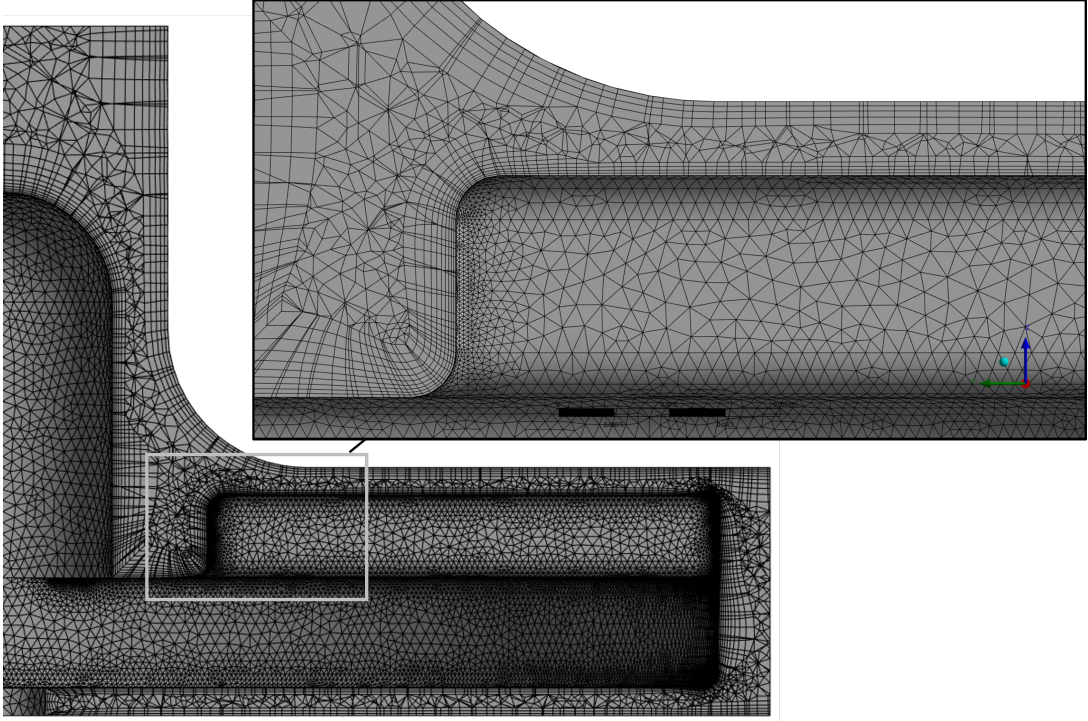


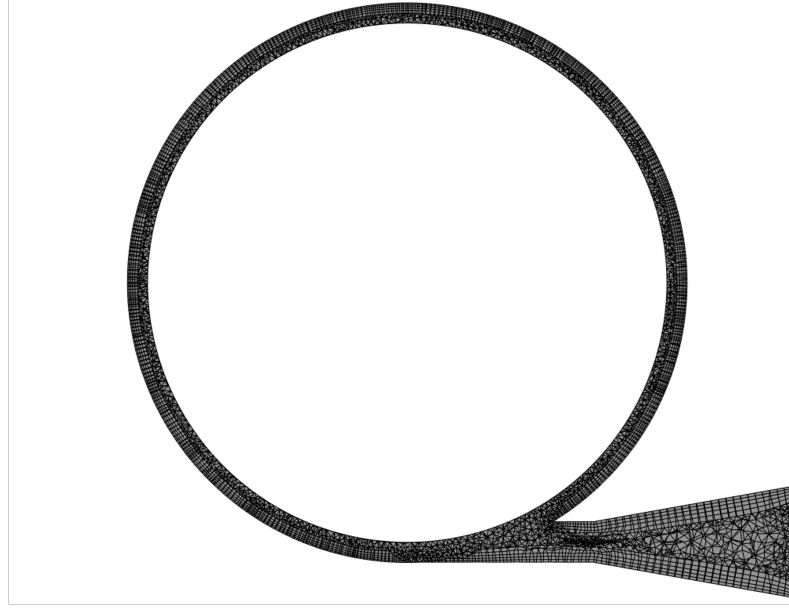
Figure 4: The rotor mesh topology generated using tetrahedral and prismatic elements.

The exit was meshed with a combination of tetrahedral, hexahedral, and prismatic elements. Tetrahedral elements were used in the remaining volume of the rotor and in the diffuser (Figure 5(a)). The element sizes at the rotor-exit interface were kept similar. Since the exit is a straight pipe, hexahedral elements were used and these were generated such that the hexahedral and tetrahedral elements were conformal (Figure 5(b)).

In addition to this initial mesh, a coarser, and two finer meshes were constructed to assess discretisation errors. These were made by multiplying the element size parameter of the initial mesh by 0.5 (Coarse mesh), 1.414 (Fine 1 mesh), and 2 (Fine 2 mesh). The actual refinement ratio (r), was calculated from the number of elements in the finer mesh (N_{fine}), and the number of elements in the coarser mesh (N_{coarse}) by

$$r = \left(\frac{N_{fine}}{N_{coarse}} \right)^{(1/3)}. \quad (2)$$

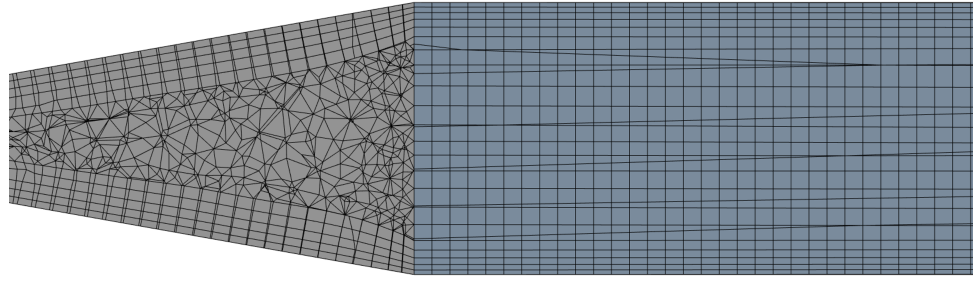
Details of these grids are summarised in Table 1. The effect of y^+ was also studied by generating grids with larger and smaller y^+ values. This was done by modifying the number of prism layers generated whilst still adopting the smooth transition approach to inflation layer generation on the eventual grid selected as outlined in Section 2.3.



(a)

Diffuser

Exit Pipe



(b)

Figure 5: The exit mesh topology generated using tetrahedral elements (a) in the remaining rotor housing, hexahedral elements in the exit pipe (b), and prismatic elements at the walls.

Table 1: Details of the grids for the grid independence study

Grid	Rotor Element Size ($\times 10^{-3}$ m)	Cells ($\times 10^{-6}$)	r (-)	$y_{avg}^+ \left(\begin{array}{c} y_{max}^+ \\ y_{min}^+ \end{array} \right)$
Coarse	1.0	1.64	-	9.26 $\left(\begin{array}{c} 27.8 \\ 0.15 \end{array} \right)$
Medium	0.50	1.86	1.04	7.63 $\left(\begin{array}{c} 13.8 \\ 0.17 \end{array} \right)$
Fine 1	0.397	2.21	1.06	6.83 $\left(\begin{array}{c} 12.0 \\ 0.093 \end{array} \right)$
Fine 2	0.25	3.89	1.21	5.39 $\left(\begin{array}{c} 8.91 \\ 0.14 \end{array} \right)$

2.2 Numerical Modelling Procedure

The incompressible Navier-Stokes equations were solved using Ansys CFX, which is a commercial finite volume method solver. The pump was modelled as a steady-state system with stationary reference frames for the inlet and outlet pipes and rotor housing, and a rotating reference frame for the rotor. Frozen rotor interfaces between the rotating and stationary reference frames were employed which maps variables directly onto neighbour patches. In reality, the flow field will be highly unsteady due to the rotation of the rotor changing the proximity of the blades to the entrance to the diffuser. Due to the limited time-frame and the fact simulations were performed on a desktop workstation, modelling the full transient nature of the problem using a sliding mesh interface was deemed too computationally demanding. The high-resolution advection scheme was used to maximise the order of spatial discretisation.

The Reynolds number (Re_{inlet}) in the inlet varies from $1.3\text{--}3.7 \times 10^3$, while the rotor Reynolds number (Re_{rotor}), which is given by

$$Re_{rotor} = \frac{\rho \Omega D_{rotor}^2}{\mu}, \quad (3)$$

where ρ is the fluid density, Ω is the pump angular speed, D_{rotor} is the rotor diameter, and μ is the dynamic viscosity, varies from $2.1\text{--}2.9 \times 10^5$ [8]. Although transition should occur at $Re \approx 10^6$, implying the flow should be fully laminar, the complex flow which occurs in VADs means the flow is likely to be in the low Re turbulent regime [1]. The $k - \omega$ Shear Stress Transport (SST) turbulence model [13] was therefore used as it has been employed by the majority of studies of the FDA benchmark blood pump [8, 10] and has been found to give accurate predictions for pressure head in VADs [1].

For each simulation, convergence was determined by the pressure head, and average WSS in the rotor and exit domains reaching stable values, and the momentum, turbulence, and continuity residuals being below 10^{-3} [1].

Blood was modelled as an incompressible fluid with density 1035 kg/m^3 and as Newtonian with dynamic viscosity 0.0035 Pa s initially. To assess the effect of shear-thinning rheology on the flow and likelihood of thrombosis, it was subsequently modelled with the Carreau viscosity model given by

$$\mu = \mu_\infty + (\mu_0 - \mu_\infty) [1 + (\lambda \dot{\gamma}^2)]^{\frac{n-1}{2}} \quad (4)$$

where μ_∞ is the high-shear viscosity, (0.0035 Pa s), μ_0 is the zero-shear rate viscosity (0.056 Pa s), λ is the time constant (3.313 s), and n is 0.3568 [14].

Table 2: Operating conditions of the blood pump tested [8].

Condition	Flow Rate (l/min)	Pump Speed (rpm)	Newtonian (y/n)	Carreau (y/n)
1	2.5	2500	y	y
2	2.5	3500	y	y
3	4.5	3500	y	n
4	6.0	2500	y	y
5	6.0	3500	y	n
6	7.0	3500	y	n

The Newtonian viscosity model calculations were performed for the six conditions for which PIV data is available from <https://ncihub.cancer.gov/wiki/?version=>. These conditions are summarised in Table 2. The inlet boundary condition was a uniform mass-flow inlet, while the outlet was set to uniform zero pressure. All walls were treated with the no-slip condition and the rotor rotational speed was varied with the pump speeds as in Table 2. The non-Newtonian model was run on Conditions 1, 2, and 4 to assess the impact of shear-thinning with flow rate and pump speed.

2.3 Grid Independence and y^+ Study

2.3.1 Grid Independence Study

The four grids shown in Table 1 were solved for Condition 1. The values for pressure head, average rotor WSS, and average exit WSS were averaged over the final 25 of 500 iterations performed for each grid. Errors for the pressure head were computed based on the experimental value obtained of 153 mmHg. For the average WSSs, the errors were estimated using Richardson's extrapolations outlined by Roache [15]. The error in the result of the finer of two grids, E_{coarse} , can be estimated from the difference in the value between the coarser and finer grids, ε , the refinement ratio, r , and the order of accuracy of the solution algorithm by

$$E_{fine} = \frac{\varepsilon}{1 - r^p}. \quad (5)$$

The error in the coarser grid result, E_{coarse} , is given by

$$E_{coarse} = \frac{r^p \varepsilon}{1 - r^p}. \quad (6)$$

A second order discretisation scheme was assumed (i.e. $p = 2$). In reality, the high-resolution scheme used blends between the second order accurate central differencing and first order accurate upwind schemes meaning the scheme is not exactly second order accurate. The errors are expressed as a percentage of the experimental value in the pressure head case, and as a percentage of the value from the

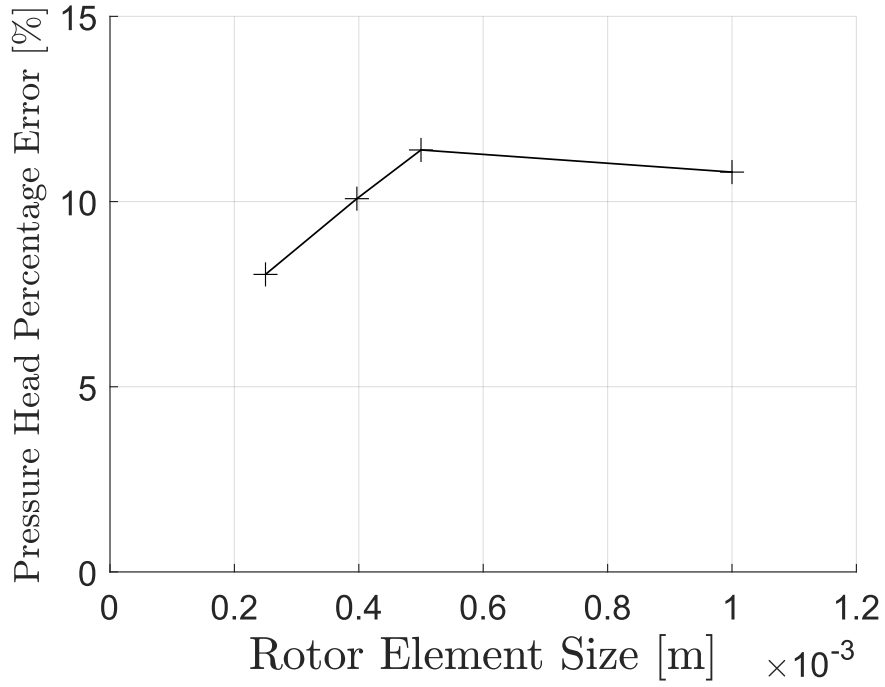


Figure 6: Pressure head error against rotor element size.

grid in the average WSS cases. These errors were then plotted against rotor element size (see Table 1). Figure 6 shows the pressure head error varying between 11.4 % for the medium mesh and 8.03 % for the Fine 2 mesh. The error for the coarse mesh (10.8 %) is unexpectedly lower than the medium mesh. This is likely because the complex flow field causes the grid convergence to be oscillatory rather than being completely monotonic. The mesh quality of the the coarse mesh was also significantly poorer as inflation layers could not generate in the gap between the rotor and bottom of the casing with the rotor element size used as Figure 7 shows. Between the medium and Fine 2 grid, the pressure head error decreases at a near constant rate implying these grids are in the asymptotic range of convergence.

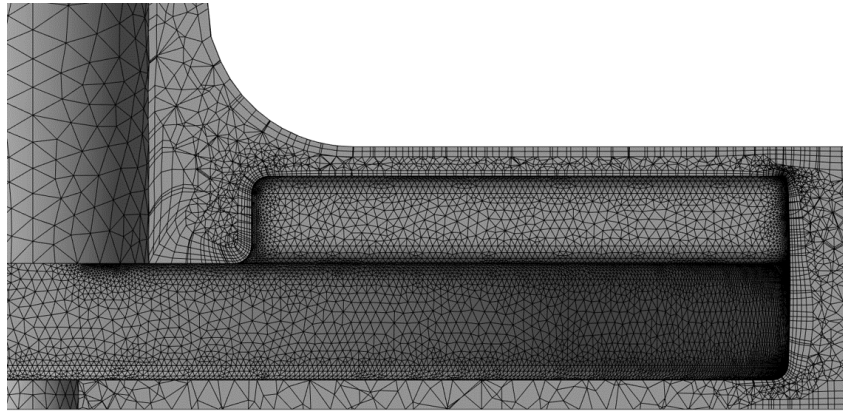


Figure 7: Clearance gap between the bottom surface of the rotor and the bottom surface of the casing in the coarse mesh.

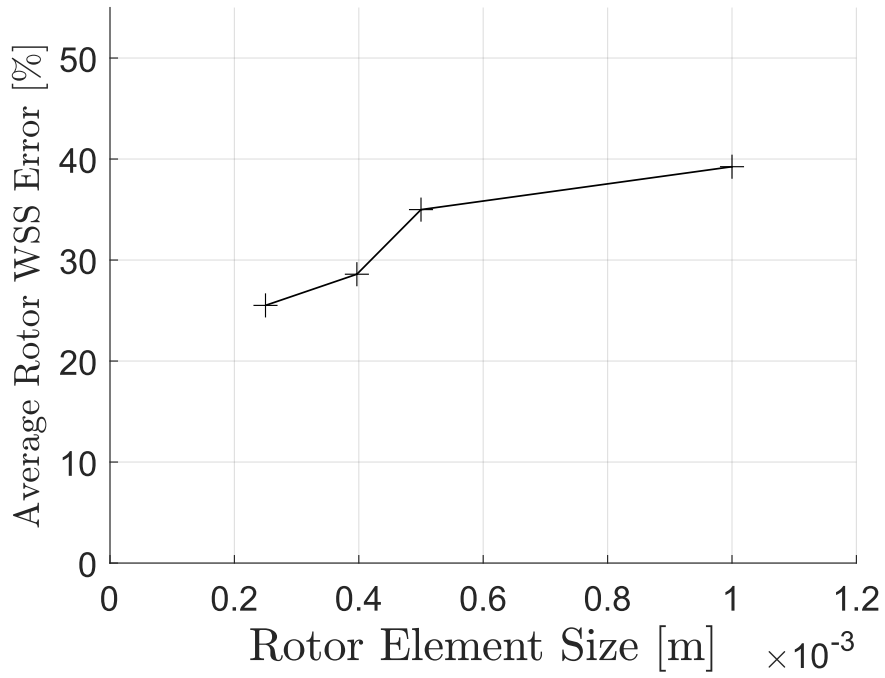


Figure 8: Average rotor WSS against rotor element size.

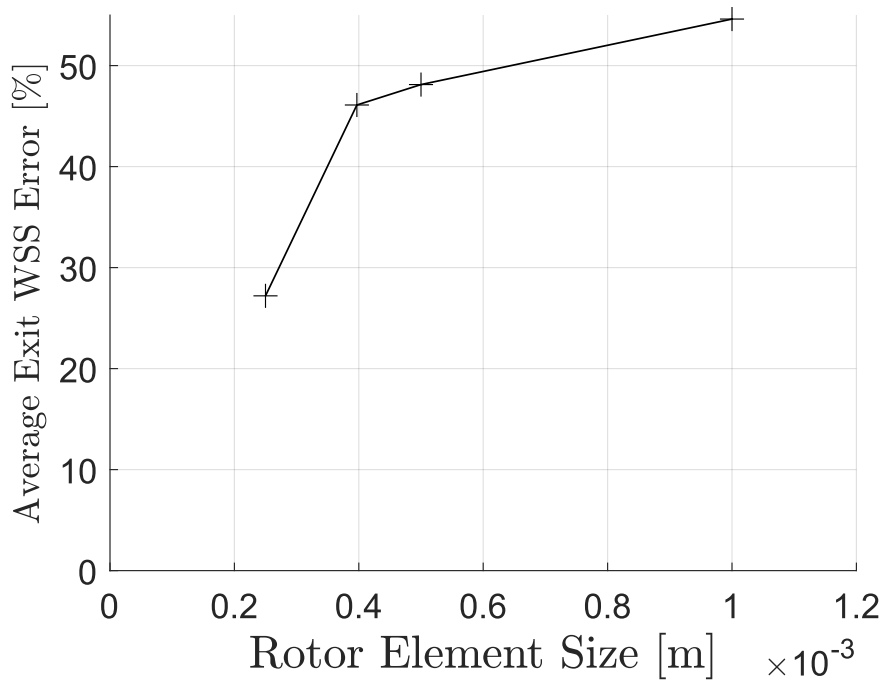


Figure 9: Average exit WSS against rotor element size.

Table 3: Details of the grids generated for the y^+ study.

Grid	Number of Layers	Cells ($\times 10^6$)	$y_{avg}^+ \left(\begin{array}{c} y_{max}^+ \\ y_{min}^+ \end{array} \right)$
High y^+	3	2.07	9.23 $\left(\begin{array}{c} 16.3 \\ 0.23 \end{array} \right)$
Initial y^+	5	2.21	6.83 $\left(\begin{array}{c} 12.0 \\ 0.093 \end{array} \right)$
Low y^+	10	2.71	3.06 $\left(\begin{array}{c} 5.75 \\ 0.0774 \end{array} \right)$

The rotor average WSS error decreases monotonically with rotor element size as shown in Figure 8. Between the medium and Fine 2 grid, errors decrease close to a constant rate giving further evidence that these are within the asymptotic range. By contrast, Figure 9 shows the average exit WSS decreases at a constant rate between the Coarse and Fine 1 grids before increasing between the Fine 1 and Fine 2 grids. Although the Fine 2 mesh consistently produced the smallest errors, the Fine 1 mesh was selected for the y^+ study and beyond as it was consistently in the asymptotic range of convergence and would take less time to solve. Given the fact that all six conditions needed to be run with the Newtonian viscosity model followed by four conditions with the non-Newtonian model (as well as the remaining y^+ study), the Fine 2 mesh would not be feasible for use.

2.3.2 y^+ Study

From the selected Fine 1 grid, two grids were generated to assess the effect of y^+ on the average rotor WSS. The number of inflation layers generated was varied from five (initial Fine 1 mesh) to three for the high y^+ case, and to ten for the low y^+ case. The details of these grids is summarised in Table 3. The low y^+ grid was the only grid where the average y^+ was less than five, which is the limit of the viscous sublayer. Ideally the entire rotor would have a y^+ less than one. This would mean that the first cell half-height is equal or less than the smallest turbulence length scale and the WSS can be accurately computed. Above this value, a wall function is used which extrapolates flat-plate correlations to determine WSS. In the viscous sublayer, the non-dimensional velocity, u^+ , is given by

$$u^+ = y^+, \quad (7)$$

while in the log layer, where y^+ is greater than 30, it is given by

$$u^+ = \frac{1}{\kappa} \ln y^+ + C^+, \quad (8)$$

where κ is the von Karman constant and C^+ is a constant of proportionality.

The average WSS was plotted against average rotor y^+ in Figure 10. This shows significant changes in the average rotor WSS with decreasing y^+ implying this has a significant effect. Since thrombosis is

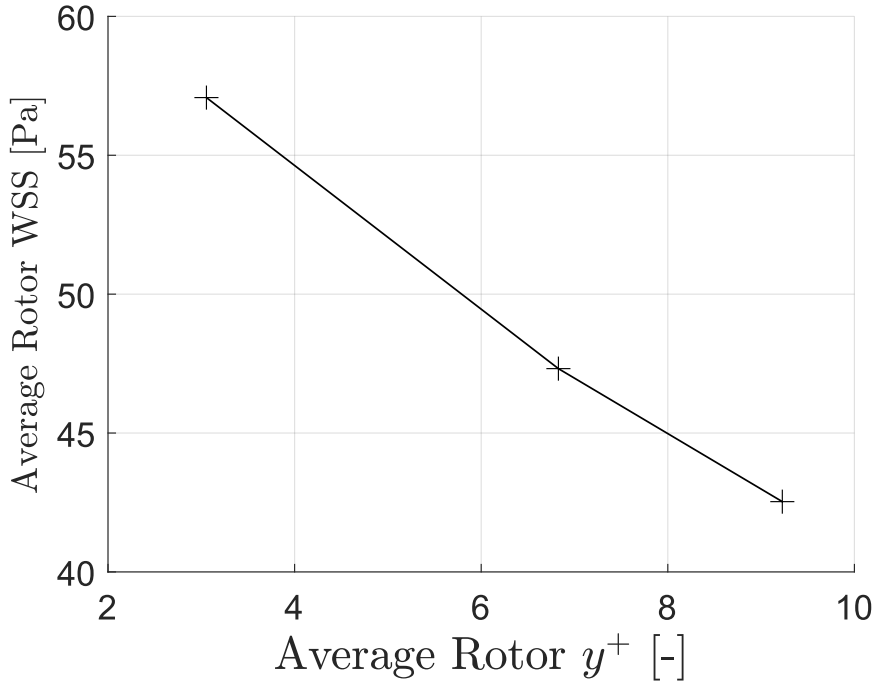


Figure 10: Average rotor WSS against y^+ value.

heavily linked to WSS, the low y^+ grid was taken forward for the rest of the simulations. Ideally, the y^+ would be reduced even further, but this would increase the number of elements which would result in excessive computation time.

2.4 Numerical Model Validation

The CFD simulations were validated against the pressure head measured by experiment by Malinauskas et al [11] and the velocity field measured from PIV experiments by Hariharan et al [12] for each condition.

2.4.1 Validation using FDA Pressure Head Data

The pressure heads measured from the CFD simulations for each pump speed (2500 rpm and 3500 rpm) were plotted with the experimentally measured values [11] against volume flow rate in Figure 11. At 2.5 l/min, there is good agreement between CFD and experiment with CFD overpredicting pressure head with percentage errors of 10 % and 5 % for 2500 rpm and 3500 rpm respectively. CFD predicts the the correct trends in pressure head with flow rate for both rotor speeds. The pressure head decreases with flow rate with an increasing (i.e. more negative) gradient. However, it underpredicts the rate of loss of pressure head leading to larger errors of 78 % and 61 % for 2500 rpm and 3500 rpm respectively at their highest flow rates. These discrepancies are likely due to the remaining discretisation errors and the steady-state assumption. It is promising, however, that the global trends are captured with this

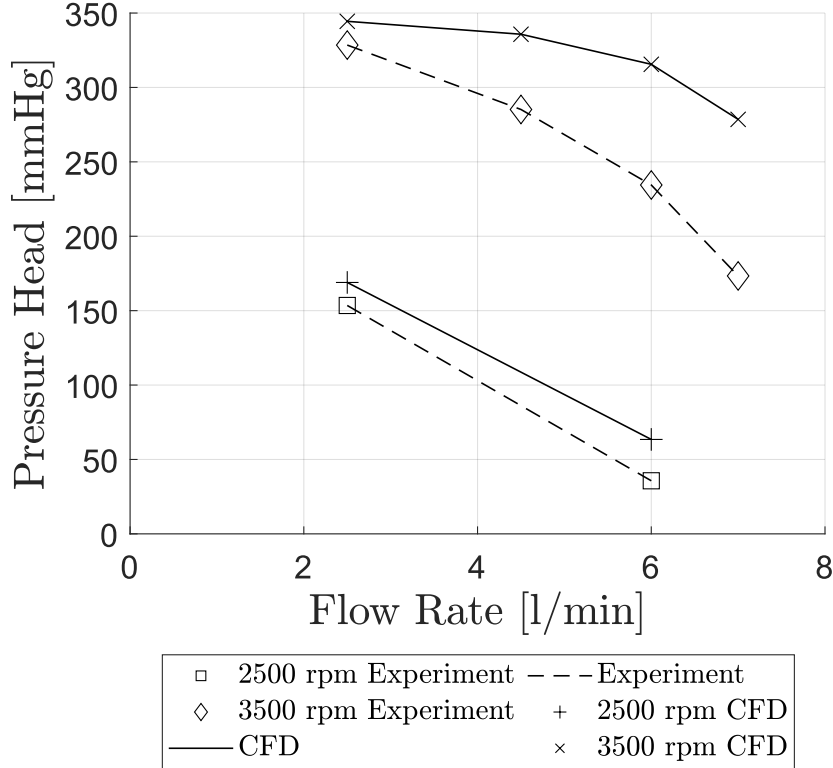


Figure 11: Pressure head against volume flow rate for the FDA blood pump comparing experimental and CFD derived values.

simplified model.

2.4.2 Validation using FDA PIV Data

Contour plots of velocity from the PIV data for the second quadrant and the diffuser have been provided by Ponnaluri et al. [8] for Conditions 2, 4, and 5. These have been compared to the respective CFD solutions in Figure 12. The CFD results show reasonable qualitative agreement with PIV - in all three cases the jet entering the diffuser is attached to the correct side as the experiments. There is an overprediction of velocity in the jet in the distal region, however. The velocity near the wall of the rotor housing is higher in the PIV measurements, particularly in Condition 4, and the low velocity regions at low radius are smaller in the experiments.

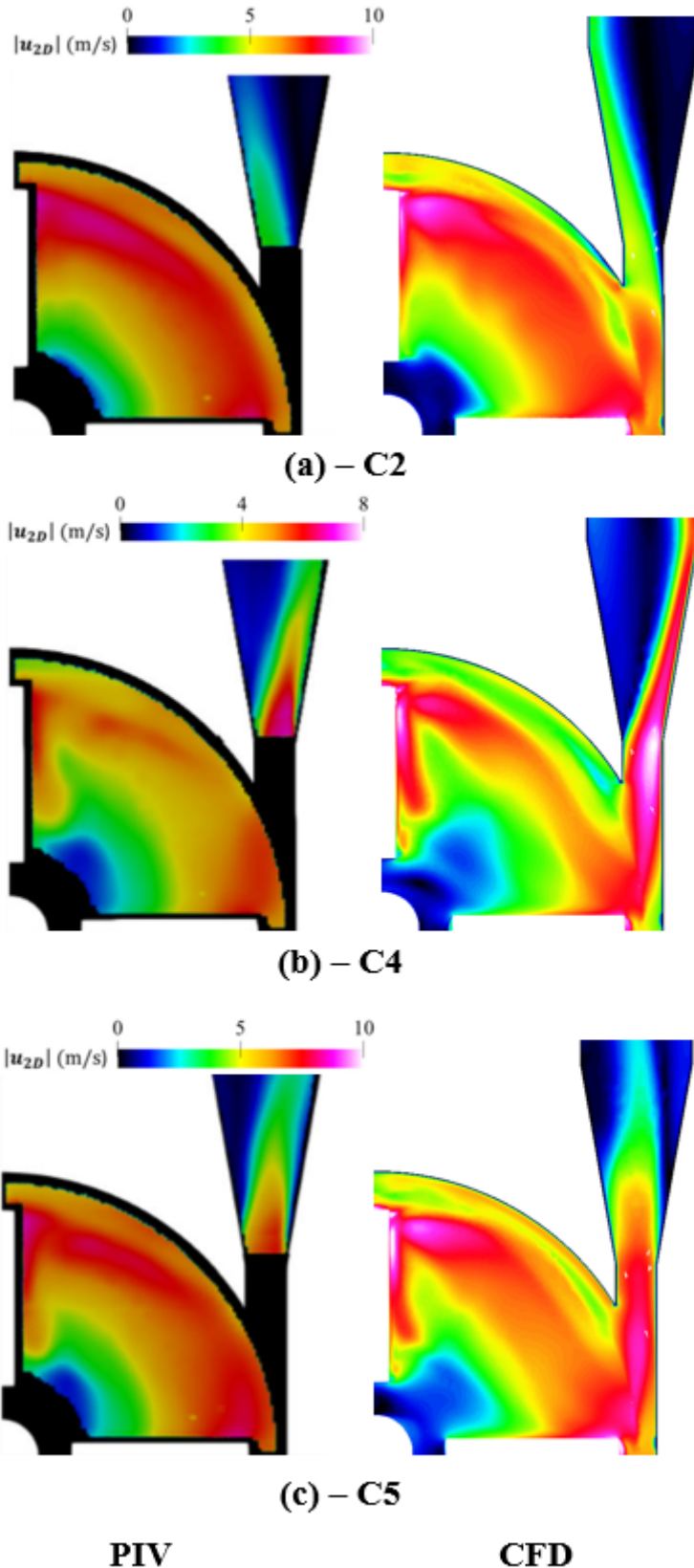


Figure 12: Comparison of velocity contours for PIV (left) and CFD (right) for Conditions 2 (a), 4 (b), and 5 (c)

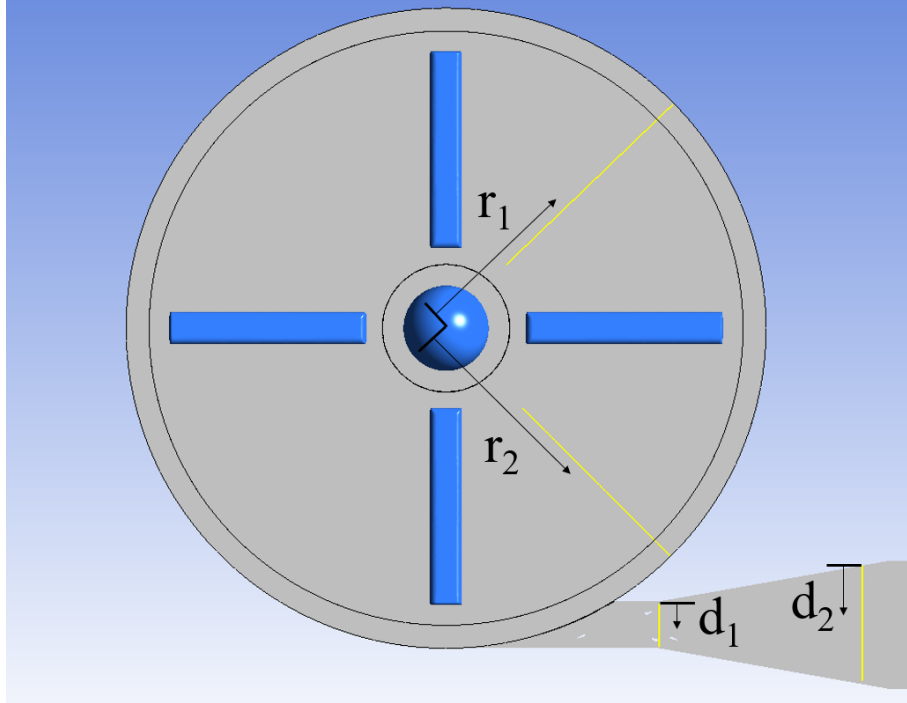


Figure 13: Lines on which velocity was plotted to validate against the PIV experiments by Hariharan et al. [12]

To quantitatively validate the numerical model, the velocity was plotted on lines at the 45° angles of quadrants 1 and 2, yielding the distances r_1 and r_2 , as well as on lines at the diffuser entrance and exit giving d_1 and d_2 as shown in Figure 13.

Figure 14 shows that in the first quadrant, Conditions 1–3, corresponding to low flow rate, have good agreement at low radii. The peak velocity is overestimated by CFD but its location is captured well. At the radii beyond the peak, the local minima in velocity are lower than the PIV measurements. The higher flow rate conditions (4–6) maintain the good agreement at low radii and the trough in velocity is similarly overpredicted, however the peak velocity occurs at a lower radius than the experiments.

The velocity profiles for the second quadrant are shown in Figure 15. The predicted velocity is consistently lower than in PIV across all pump speeds and flow rate. The velocity deficit increases with flow rate. The diffuser entrance velocity profiles are plotted in Figure 16. Conditions 1–2 show higher velocity at low distances and tend towards the PIV results at the higher distances. Condition 6 distribution shape is not as flat as PIV suggests. The diffuser exit velocity profiles given in Figure 17 show large overpredictions of the maximum velocity by a factor of approximately two in all conditions where PIV is available. It should be noted that this error is similar in Good and Manning [10] (see Figure 6 of ref [10]). For Conditions 1–2, the maxima are located at a lower distance than in PIV but the Condition 6 maximum is accurate. The lower velocities are well predicted, however.

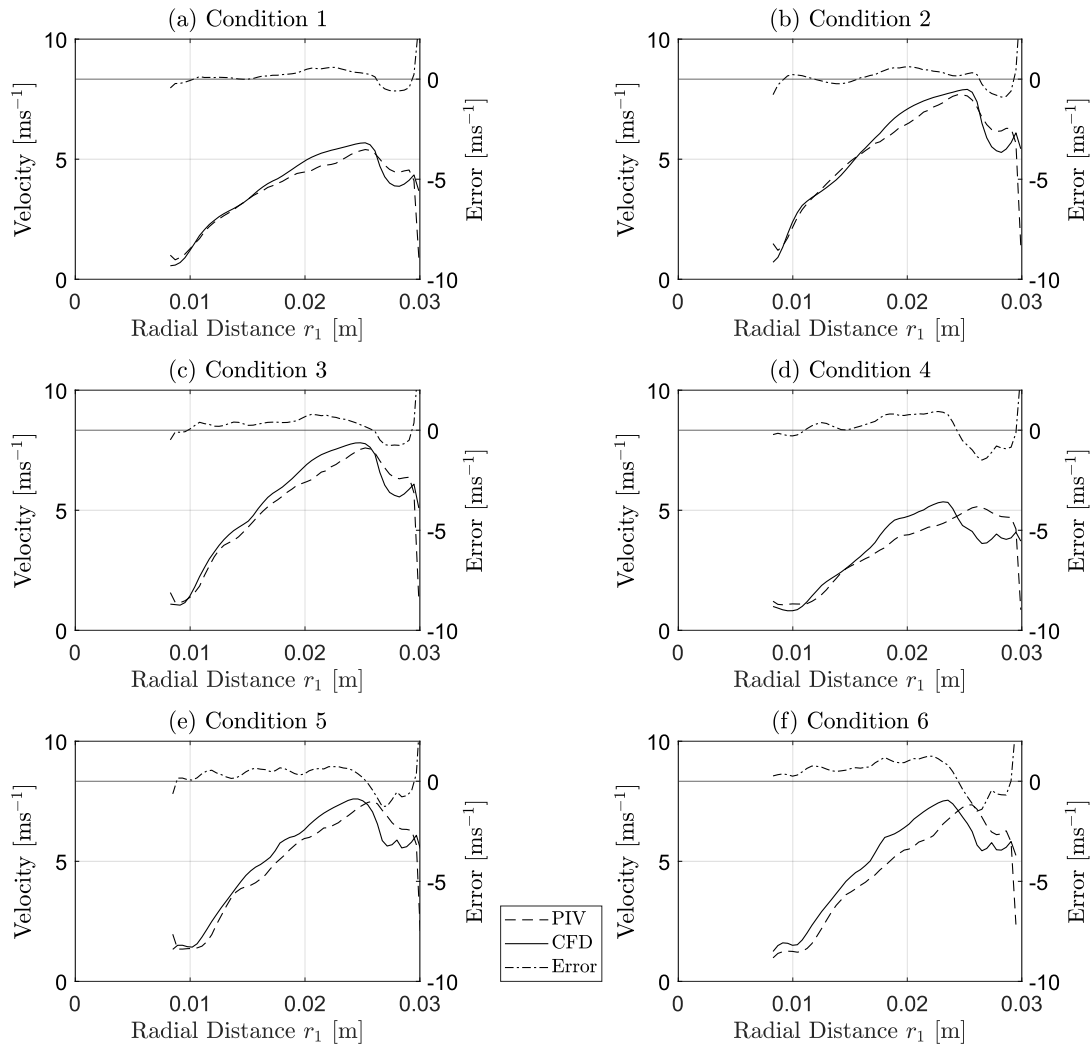


Figure 14: Velocity profiles along the r_1 line compared between CFD and PIV for all six conditions.

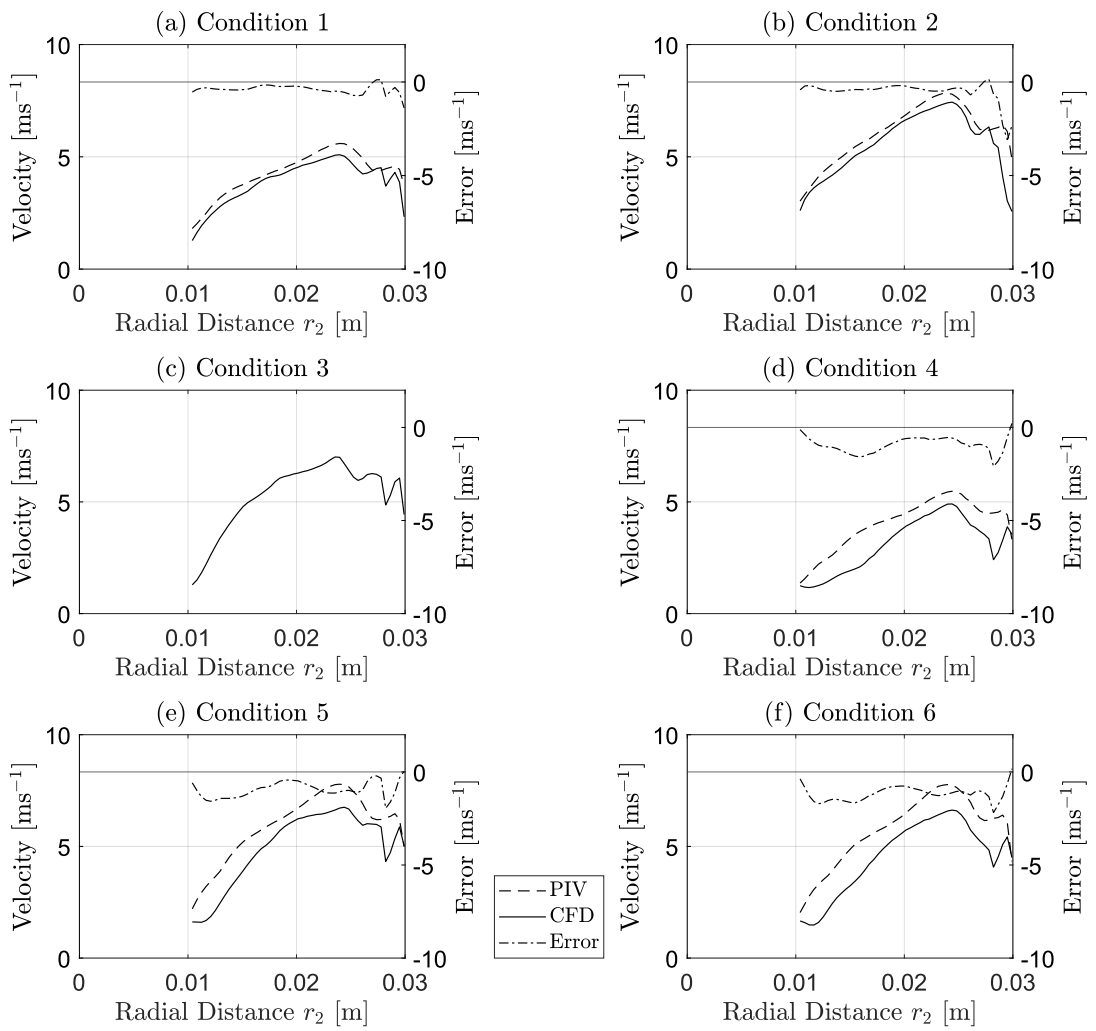


Figure 15: Velocity profiles along the r_2 line compared between CFD and PIV for all six conditions.

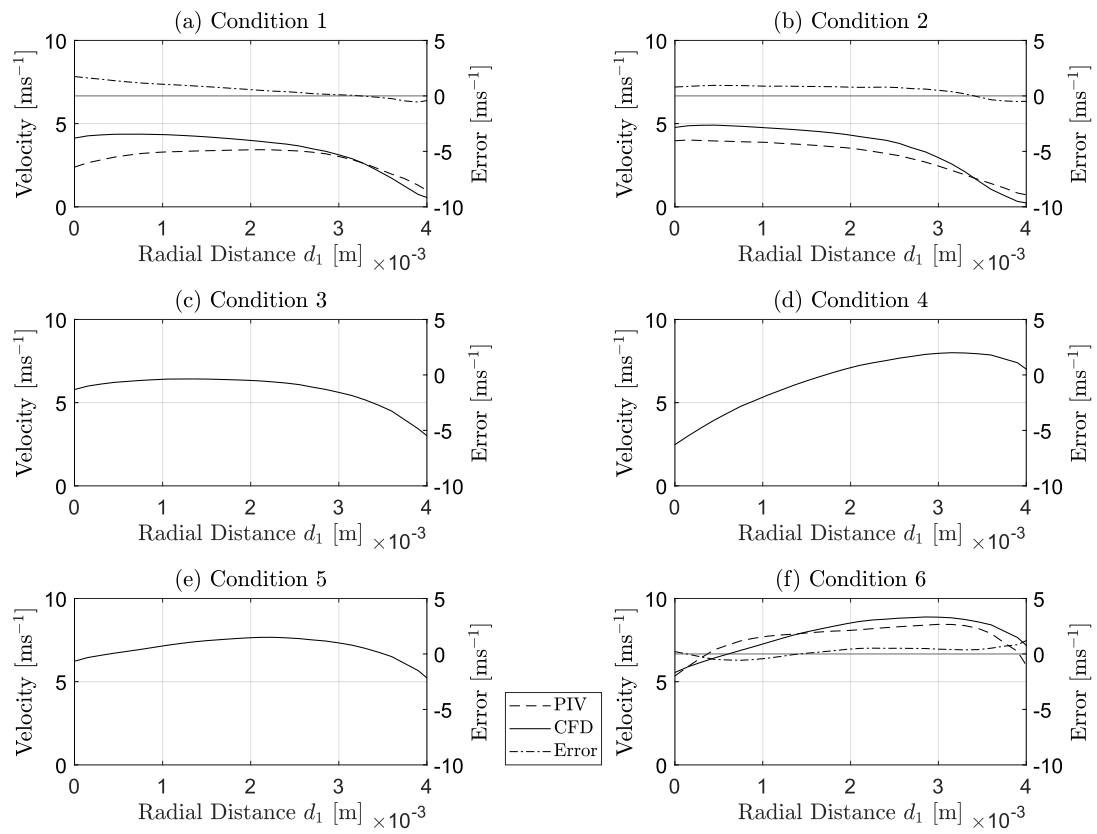


Figure 16: Velocity profiles along the d_1 line compared between CFD and PIV for all six conditions.

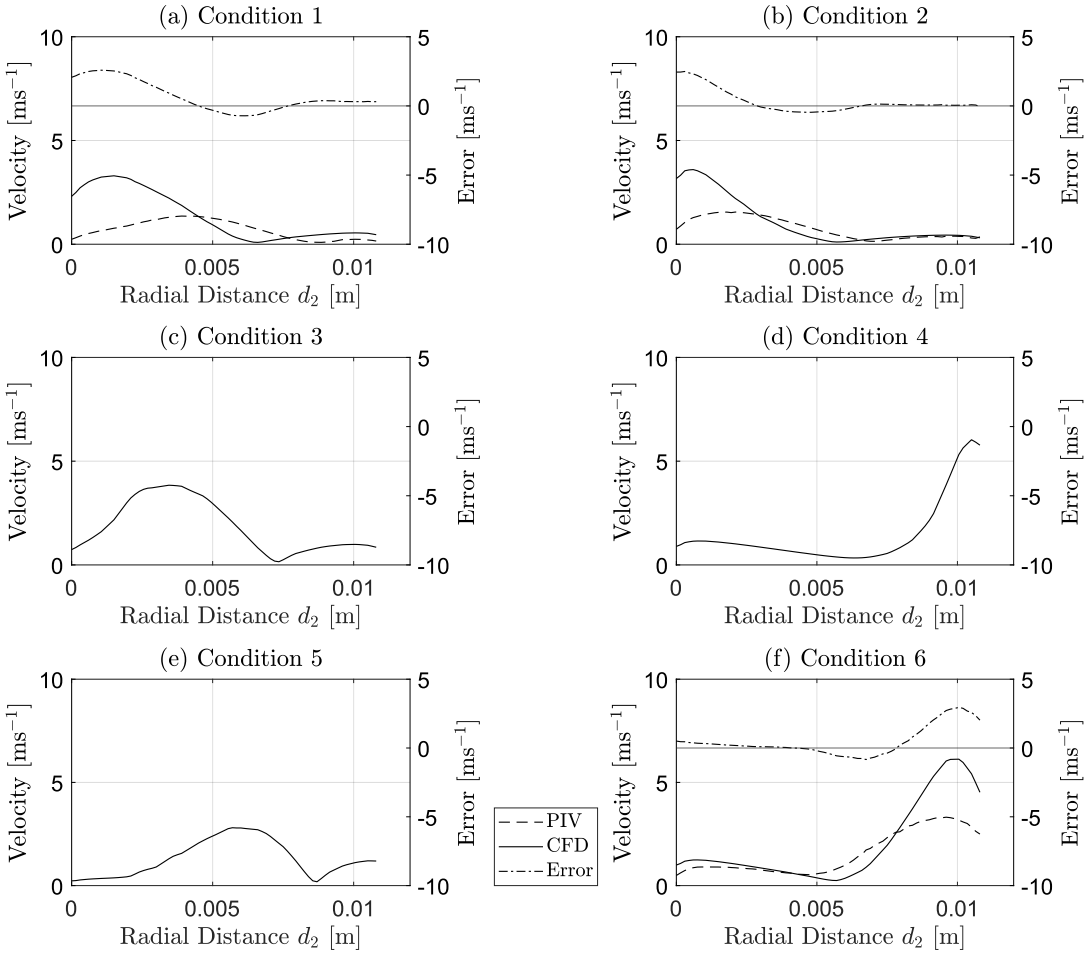


Figure 17: Velocity profiles along the d_2 line compared between CFD and PIV for all six conditions.

3 Results and Discussion

The effect of a shear-thinning Carreau rheology model was investigated with respect to the velocity distributions in the rotor, diffuser, as well as the inlet. The likelihood of thrombosis formation was then compared between the rheological models.

3.1 Shear-Thinning Effects on Inlet and Exit Dynamic Viscosity

The dynamic viscosity in the bulk flow at the distal end of the exit is increased with the Carreau model (Figure 18), as it is in the inlet (Figure 19). This is due to the low velocity gradients, and so low shear rates in fully developed bulk-flow.

The radial velocity distribution was plotted 50 mm proximal to the rotor in Figure 20 with velocity normalised to the average velocity in the inlet. The shear-thinning model shows a marginally sharper

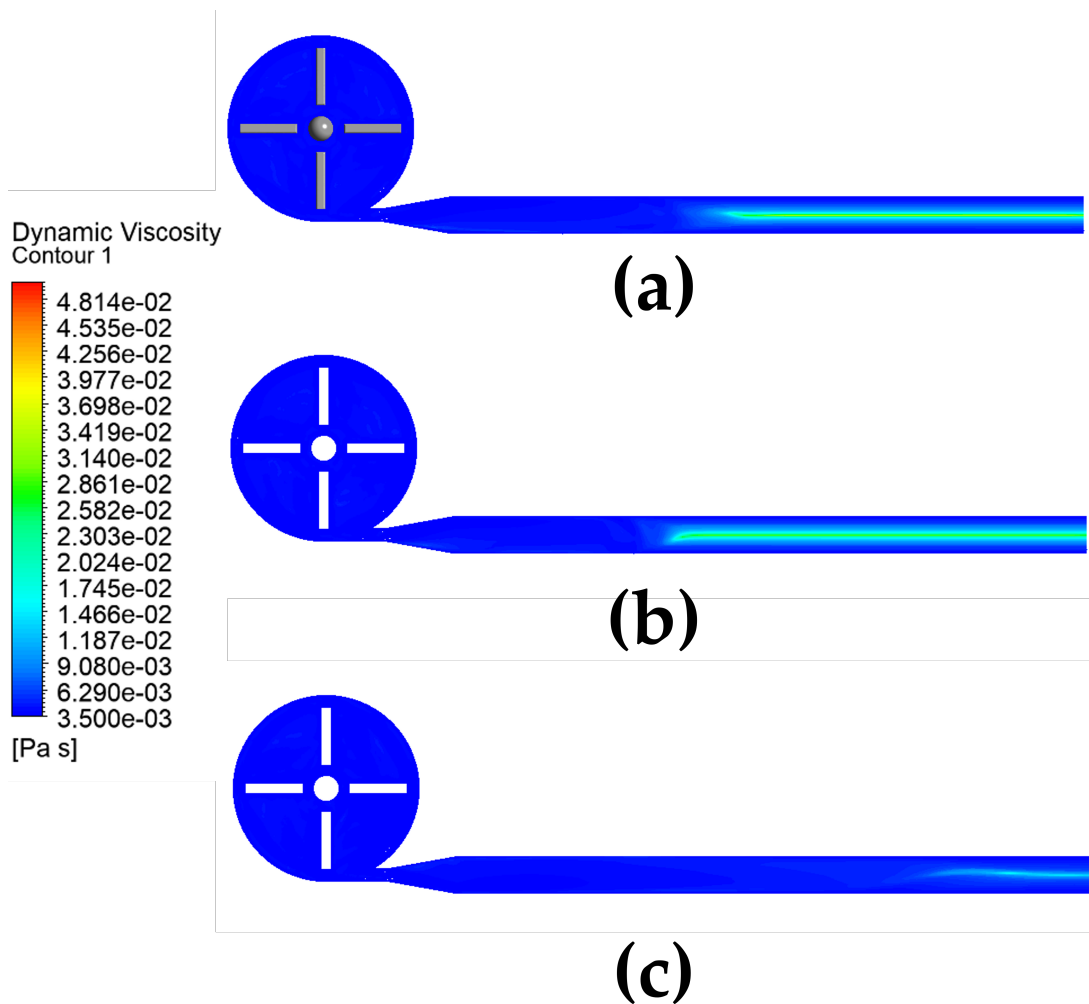


Figure 18: Dynamic viscosity contour in the rotor and exit of the pump for Conditions 1 (a), 2 (b), and 4 (c).

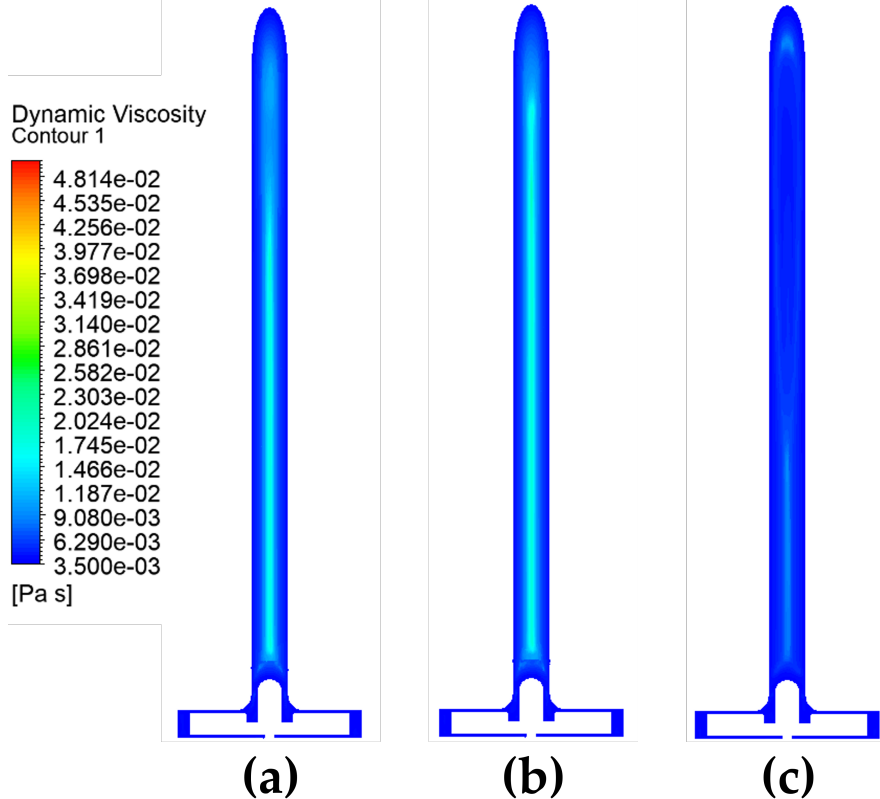


Figure 19: Dynamic viscosity contour in the rotor and inlet of the pump for Conditions 1 (a), 2 (b), and 4 (c).

profile with a larger peak velocity for Conditions 1–2. Experiments by Gisjen et al. [16] would suggest that the non-Newtonian profile should be flatter. However, these experiments were conducted in the laminar regime. The SST model used here means that the profile will be a turbulent one. Therefore, since shear-thinning fluids tend to undergo transition [17] as the effective Re is reduced by the increased dynamic viscosity, the profile of the non-Newtonian model approaches that of a laminar one (although it is still a turbulent profile). In Condition 6, where flow rate is high, the profiles are almost identical. This is likely due to the increased global Re dominating.

3.2 Comparison of Velocity Fields in Newtonian and Shear-Thinning Models

The rheological model used made negligible impact on the velocity distributions in the rotor and diffuser as Figure 21 shows. There was minor differences in the low radii values for the high-flow condition (Condition 4) where the shear-thinning model predicted slightly higher velocities. This contrasts the findings of Good and Manning [10], who found significant differences in the diffuser exit velocity profiles when incorporating a viscoelastic rheological model. This suggests that in blood pumps, viscoelastic effects may dominate over shear-thinning effects.

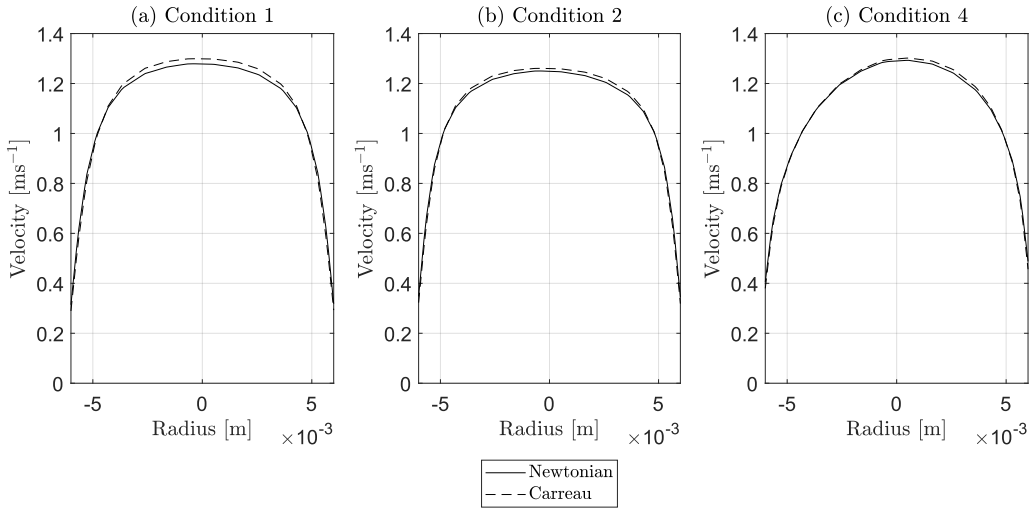


Figure 20: Radial velocity profiles of the inlet pipe 50 mm proximal to the rotor normalised by the average velocity in the pipe for Conditions 1 (a), 2 (b), and 4 (c).

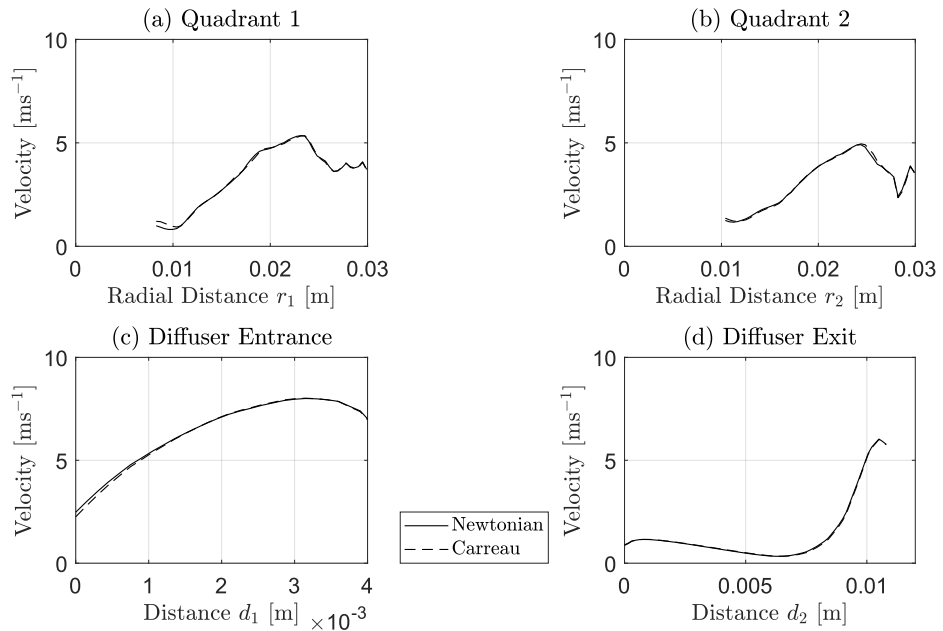


Figure 21: Velocity distributions for the Newtonian and Carreau models in the first two quadrants of the rotor and the entrance and exit of the diffuser for Condition 4.

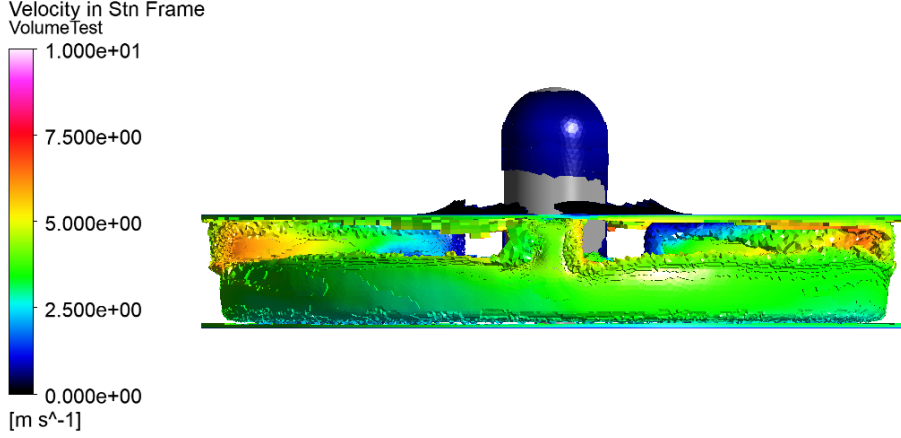


Figure 22: Iso-volume coloured by velocity of shear rate greater than the threshold value for platelet activation (2570 s^{-1}).

3.3 Effects of Shear-Thinning Rheology on Thrombosis

For thrombosis to occur, platelets must be activated by high shear rates and then deposited or allowed to coagulate by low shear rate. Since the inlet does not cause high shear rates due to the lack of moving parts, it was excluded from this part of the analysis as the rotor is the dominant factor behind platelet activation. The threshold for platelet activation was set to 9 Pa of scalar shear stress [1]. From Equation 1, and assuming the continuum value of dynamic viscosity of 0.0035 Pa, the critical shear rate for platelet activation is approximately 2570 s^{-1} . Since this is a very high shear rate, shear-thinning effects will be negligible and so focus is placed on changes in platelet deposition regions. For platelet deposition, a threshold shear rate of 250 s^{-1} was used following findings by Hochareon et al. [7], who showed areas of shear rate below this value coincided with thrombus formation of the 50 cc Penn State Artificial Heart. The shear rate in the rotor is very high due to the large accelerations around the blades (Figure 22). This means platelets will be activated and so platelet deposition caused by low shear rate in or distal to the rotor is most likely to lead to thrombosis. Therefore the rotor and exit are the target areas of interest for low shear-rate.

Figure 23 shows low shear rate regions in the volumes between the rotor blades as well as in the diffuser region outside of the jet implying that these regions may be prone to thrombus formation. Thrombosis in the rotor could reduce its performance and so reduce the pressure head of the pump. If this is allowed to build up to a significant degree, the VAD may need a complete replacement. Thrombus in the diffuser section may be dislodged and travel to distal arteries in the brain causing stroke. The regions of low shear rate are slightly reduced in size by pump speed comparing Conditions 1 (Figure 23(a)) and 2 (Figure 23(b)), but there is a more significant reduction with flow rate from comparing Conditions 1 and 4 (Figure 23(c)).

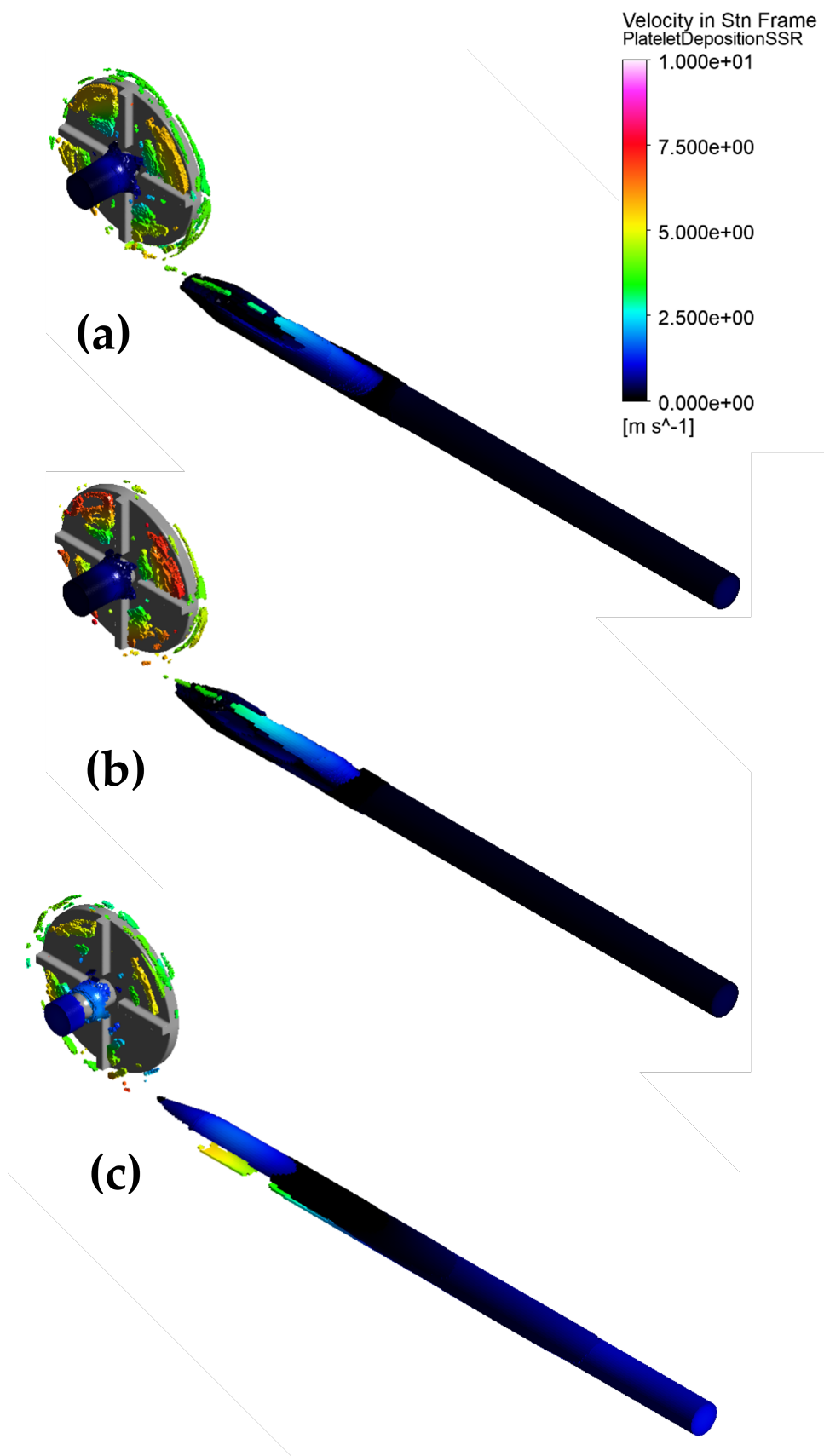


Figure 23: Iso-volumes coloured by velocity of shear rate less than the threshold value for platelet deposition in the rotor and exit for Conditions 1 (a), 2 (b), and 4 (c). N.B. only the Newtonian cases are shown as visible differences are negligible between rheological model.

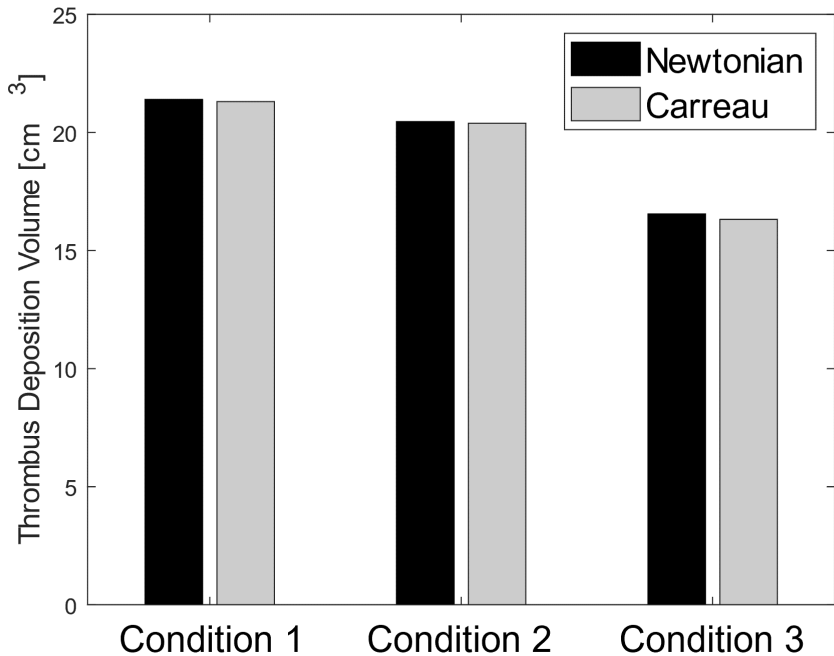


Figure 24: Volume of blood in the rotor and exit below the shear rate threshold of platelet deposition compared between the Newtonian and Carreau models.

The volume of regions prone to thrombosis predicted by the Newtonian and shear thinning models for each conditions are plotted in Figure 24. This clearly shows the importance of the low pump speed, low flow rate condition. The shear thinning model predicts a slightly reduced thrombosis potential across the conditions with the largest effect being in Condition 4 (high flow rate) in both absolute (0.2 cm^3) and percentage (1.4 %) terms. In the low flow rate conditions (1–2), the reduction in low shear volume is similar at 0.1 cm^3 (0.4 % and 0.3 % respectively). Since the risk of thrombosis is greatest at low pump speed and low flow rate conditions and the Newtonian viscosity model is more conservative, it can be concluded that shear thinning rheology has a limited effect on thrombosis estimation in the FDA blood pump. The findings of Good and Manning [10] suggest that viscoelasticity may have an effect on thrombosis since it was shown to have greater sensitivity at low pump speed and flow rate.

4 Conclusions

Steady-state multi-reference frame simulations were conducted on the FDA centrifugal blood pump model for all six conditions for which PIV velocity field data was provided under a Newtonian viscosity assumption. Simulations were then performed under a shear thinning Carreau viscosity model for Conditions 1,2, and 4 to compare the low shear rate regions thought to be responsible for platelet deposition.

The velocity flow field showed good qualitative and quantitative agreement in the rotor and diffuser

entrance. The diffuser exit jet velocity was overpredicted by CFD compared to PIV, however. The pressure head followed a similar trend to the experiments with flow rate, with a increasing rate of reduction in pressure head with flow rate. However, the steady-state simulations underpredict the loss in pressure head leading to large errors. Future work should look to resolve the discretisation errors with finer grids and to assess the effect of the moving rotor blades with a fully transient simulation.

The shear rate in the rotor was very high meaning platelet activation in and distal to this component would also be high. Low shear rate regions were found in the spaces between blades and in the diffuser outside of the jet. Application of a shear-thinning model had negligible impact on the velocity distribution and a slight decrease in thrombosis. The Newtonian model is more conservative and so we conclude its use is warranted in analysis of blood pump fluid dynamics. This work took a simplified approach to thrombosis modelling by using a threshold shear rate value rather than implementing a scalar shear stress function as Fraser et al. [1] so this should be implemented to give a more accurate assessment. Future work should investigate the effect of viscoelasticity on thrombosis as this has been shown to have a larger impact on the low flow and pump speed conditions velocity fields [10].

The key findings can be summarised as follows:

- Steady-state simulations make reasonable estimations for the velocity flow field in the rotor and diffuser entrance, but not in the diffuser exit. Pressure head variation agrees with experiment qualitatively but with large errors at high flow rate.
- Thrombosis potential is greatest in the spaces between blades in the rotor and in the diffuser.
- Thrombosis potential is greatest in low flow rate and pump speed conditions. It is strongly dependent on flow rate, and weakly dependent on pump speed.
- Shear thinning rheology has negligible effect on the velocity distribution in the rotor and diffuser, and a minor reduction in thrombosis potential. Its omission in the majority of studies is therefore justified.

References

- [1] K. H. Fraser, T. Zhang, M. E. Taskin, B. P. Griffith, and Z. J. Wu, “A quantitative comparison of mechanical blood damage parameters in rotary ventricular assist devices: Shear stress, exposure time and hemolysis index,” *Transactions of the ASME. Journal of biomechanical engineering.*, vol. 134, no. 8, pp. 081 002–081 002, 2012.
- [2] Statista, “Number of diagnosed incident cases of chronic heart failure among 45+ year-olds in selected countries in 2015 and 2025,” ” 2016. [Online]. Available: <https://www.statista.com/statistics/648124/heart-failure-diagnosed-incident-cases-in-45-year-olds-by-select-country/>
- [3] L. O. Thompson, M. Loebe, and G. P. Noon, “What price support? ventricular assist device induced systemic response,” *ASAIO Journal*, vol. 49, no. 5, p. 518–526, 2003.
- [4] B. Genovese, Elizabeth A., P. Dew, Mary Amanda, M. Teuteberg, Jeffrey J. *et al.*, “Incidence and patterns of adverse event onset during the first 60 days after ventricular assist device implantation,” *The Annals of thoracic surgery*, vol. 88, no. 4, pp. 1162–1170, 2009.
- [5] W. A. Whitaker-Lea, B. Toms, J. B. Toms, K. B. Shah, M. Quader, D. Tang, V. Kasirajan, D. J. Rivet, and J. F. Reavey-Cantwell, “Neurologic complications in patients with left ventricular assist devices: Single institution retrospective review,” *World neurosurgery*, vol. 139, pp. e635–e642, 2020.
- [6] E. N. Sorensen, G. W. Burgreen, W. R. Wagner, and J. F. Antaki, “Computational simulation of platelet deposition and activation: I. model development and properties,” *Annals of biomedical engineering*, vol. 27, no. 4, pp. 436–448, 1999.
- [7] P. Hochareon, K. B. Manning, A. A. Fontaine, J. M. Tarbell, and S. Deutsch, “Correlation of in vivo clot deposition with the flow characteristics in the 50 cc penn state artificial heart: A preliminary study,” *ASAIO Journal*, vol. 50, no. 6, p. 537–542, 2004.
- [8] S. V. Ponnaluri, P. Hariharan, L. H. Herbertson, K. B. Manning, R. A. Malinauskas, and B. A. Craven, “Results of the interlaboratory computational fluid dynamics study of the fda benchmark blood pump,” *Annals of biomedical engineering*, vol. 51, no. 1, pp. 253–269, 2023.
- [9] R. M. Roeck and M. R. Mackley, “The rheology and microstructure of equine blood.” [Online]. Available: <http://www.de-roeck.co.uk/Research.htm>
- [10] B. C. Good and K. B. Manning, “Computational modeling of the food and drug administration’s benchmark centrifugal blood pump,” *Artificial organs*, vol. 44, no. 7, pp. E263–E276, 2020.
- [11] R. A. Malinauskas, P. Hariharan, S. W. Day *et al.*, “Fda benchmark medical device flow models for cfd validation,” *ASAIO Journal*, vol. 63, no. 2, p. 150–160, 2017.

- [12] P. Hariharan, K. I. Aycock, M. Buesen, S. W. Day, B. C. Good, L. H. Herbertson, U. Steinseifer, K. B. Manning, B. A. Craven, and R. A. Malinauskas, “Inter-laboratory characterization of the velocity field in the fda blood pump model using particle image velocimetry (piv),” *Cardiovascular engineering and technology*, vol. 9, no. 4, pp. 623–640, 2018.
- [13] F. R. Menter, “Two-equation eddy-viscosity turbulence models for engineering applications,” *AIAA journal*, vol. 32, no. 8, pp. 1598–1605, 1994.
- [14] K. M. Saqr, O. Mansour, S. Tupin, T. Hassan, and M. Ohta, “Evidence for non-newtonian behavior of intracranial blood flow from doppler ultrasonography measurements,” *Medical biological engineering computing.*, vol. 57, no. 5, pp. 1029–1036, 2019.
- [15] P. J. Roache, “Quantification of uncertainty in computational fluid dynamics,” *Annual review of fluid mechanics*, vol. 29, no. 1, pp. 123–160, 1997.
- [16] F. Gijsen, F. van de Vosse, and J. Janssen, “The influence of the non-newtonian properties of blood on the flow in large arteries: steady flow in a carotid bifurcation model,” *Journal of biomechanics.*, vol. 32, no. 6, pp. 601–608, 1999.
- [17] D. Biswas, D. M. Casey, D. C. Crowder, D. A. Steinman, Y. H. Yun, and F. Loth, “Characterization of transition to turbulence for blood in a straight pipe under steady flow conditions,” *Transactions of the ASME. Journal of biomechanical engineering.*, vol. 138, no. 7, 2016.